



Cite this: *Nanoscale*, 2016, **8**, 18956

## Controlled growth of large-area anisotropic ReS<sub>2</sub> atomic layer and its photodetector application†

Xiaobo Li,<sup>a</sup> Fangfang Cui,<sup>a</sup> Qingliang Feng,<sup>b</sup> Gang Wang,<sup>c</sup> Xiaosa Xu,<sup>a</sup> Juanxia Wu,<sup>b</sup> Nannan Mao,<sup>b</sup> Xing Liang,<sup>a</sup> Zhongyue Zhang,<sup>c</sup> Jin Zhang<sup>b</sup> and Hua Xu<sup>\*a</sup>

As an anisotropic 2D layered material, rhenium disulfide (ReS<sub>2</sub>) has attracted much attention because of its unusual properties and promising applications in electronic and optoelectronic devices. However, the low lattice symmetry and interlayer decoupling of ReS<sub>2</sub> make asymmetric growth and out-of-plane growth occur quite easily; therefore, thick flake, dendritic and flower-like structures of ReS<sub>2</sub> have mostly been obtained previously. Here, we report on an approach based on space-confined epitaxial growth for the controlled synthesis of ReS<sub>2</sub> films. Using this approach, large-area and high-quality ReS<sub>2</sub> films with uniform monolayer thickness can grow on a mica substrate. Furthermore, the weak van der Waals interaction between the surface of mica and ReS<sub>2</sub> clusters, which favors surface-confined growth while avoiding out-of-plane growth, is critical for growing ReS<sub>2</sub> with uniform monolayer thickness. The morphological evolution of ReS<sub>2</sub> with the growth temperature reveals that asymmetric growth can be suppressed at relatively low temperatures. A ReS<sub>2</sub> field-effect transistor displayed a current on/off ratio of 10<sup>6</sup> and an electron mobility of up to 40 cm<sup>2</sup> V<sup>-1</sup> s<sup>-1</sup>, with outstanding photoresponsivity of 12 A W<sup>-1</sup>. This work not only promotes the large-scale employment of ReS<sub>2</sub> in high-performance optoelectronic devices, but also provides a means of controlling the unusual growth behavior of low-lattice-symmetry 2D layered materials.

Received 13th September 2016,  
Accepted 19th October 2016

DOI: 10.1039/c6nr07233j

www.rsc.org/nanoscale

## 1. Introduction

Two-dimensional (2D) layered materials with strong in-plane anisotropic properties such as rhenium disulfide (ReS<sub>2</sub>), rhenium diselenide (ReSe<sub>2</sub>) and black phosphorus have been proposed for developing new devices with promising applications in electronics, optoelectronics and thermoelectrics.<sup>1–5</sup> Unlike most 2D layered materials that have been investigated such as graphene and MoS<sub>2</sub>, which have high lattice symmetry, the lattice symmetry of ReS<sub>2</sub> is quite low.<sup>6</sup> Usually, ReS<sub>2</sub> crystallizes in a distorted octahedral (1T) crystal structure,<sup>7</sup> which gives rise to strong anisotropy in its optical and electrical

properties.<sup>8,9</sup> Furthermore, in contrast to other TMDs, ReS<sub>2</sub> exhibits an unusual interlayer decoupling feature owing to a Peierls distortion in the 1T structure.<sup>3</sup> In addition, ReS<sub>2</sub> is a direct-band-gap semiconductor (1.5 to 1.6 eV) from monolayers to bulk materials.<sup>10</sup> Recently, few-layer ReS<sub>2</sub> sheets, which exhibit quite distinct properties from those of group VI TMDs, have been used in high-performance field-effect transistors, digital inverters, and photodetectors.<sup>10–14</sup>

Although anisotropic ReS<sub>2</sub> has many promising applications, most studies of ReS<sub>2</sub> have been based on mechanically exfoliated samples.<sup>12,13</sup> Until recently, 2D ReS<sub>2</sub> flakes and monolayer films have been successfully synthesized using chemical vapor deposition (CVD) growth with Re powder and NH<sub>4</sub>ReO<sub>4</sub> molecules as the Re precursors, respectively.<sup>15,16</sup> Many efforts have been made in the preparation of 2D ReS<sub>2</sub>, but control of the crystal quality, domain size, thickness and morphology of ReS<sub>2</sub> still poses a great challenge owing to several outstanding problems. For example, the high volatility and versatile valence states of Re oxides make the controlled synthesis of high-quality ReS<sub>2</sub> films difficult. In particular, the distorted 1T structure and weaker interlayer coupling of ReS<sub>2</sub> could make asymmetric growth and out-of-plane growth occur quite easily; therefore, thick flake, dendritic and flower-like structures have mostly been observed previously for ReS<sub>2</sub> synthesized by CVD.<sup>10,16–18</sup> These specific features of ReS<sub>2</sub> pose

<sup>a</sup>Key Laboratory of Applied Surface and Colloid Chemistry, Ministry of Education, Shaanxi Key Laboratory for Advanced Energy Devices, Shaanxi Engineering Lab for Advanced Energy Technology, School of Materials Science and Engineering, Shaanxi Normal University, Xi'an 710119, P. R. China. E-mail: xuhua-nano@snnu.edu.cn

<sup>b</sup>Center for Nanochemistry, Beijing National Laboratory for Molecular Sciences, Key Laboratory for the Physics and Chemistry of Nanodevices, State Key Laboratory for Structural Chemistry of Unstable and Stable Species, College of Chemistry and Molecular Engineering, Peking University, Beijing 100871, P.R. China

<sup>c</sup>School of Physics and Information Technology, Shaanxi Normal University, Xi'an 710119, P. R. China

† Electronic supplementary information (ESI) available: Thermogravimetric analysis of ReO<sub>3</sub>, OM, SEM and AFM images, Raman, fluorescence spectra of ReS<sub>2</sub>, photoelectrical data. See DOI: 10.1039/c6nr07233j

more difficulties and challenges to its controllable preparation in comparison to that of traditional TMDs such as  $\text{MoS}_2$  and  $\text{WS}_2$ .<sup>9</sup> Furthermore, much less is known about the growth behavior of low-lattice-symmetry 2D materials, which should be different from that of high-lattice-symmetry 2D TMDs.

In this work, a large-area, high-quality uniform monolayer  $\text{ReS}_2$  film was synthesized using an approach based on space-confined CVD growth (Fig. 1a). Experimentally, volatile rhenium trioxide ( $\text{ReO}_3$ ) was used as the Re precursor to ensure the efficiency of the growth, and mica with a low surface energy was used as a substrate to achieve epitaxial growth. To achieve controllable growth, an approach based on space-confined growth was adopted by constructing a micro-reactor between two mica substrates in the CVD system. This procedure efficiently reduced the nucleation density and growth rate of  $\text{ReS}_2$  and thus favored large-area epitaxial growth. Moreover, to gain insight into the unusual growth mechanism of the low-lattice-symmetry 2D material  $\text{ReS}_2$ , the growth behavior of  $\text{ReS}_2$  on mica and  $\text{SiO}_2$  substrates was studied in detail. The results indicate that two different growth processes (out-of-plane/surface-confined) are responsible for the morphological differences in  $\text{ReS}_2$  obtained on  $\text{SiO}_2$  and mica substrates. These are determined by three key factors, which include anisotropic growth induced by the distorted 1T structure, the weak interlayer coupling in  $\text{ReS}_2$ , and the barrier energy to surface migration of the substrate. Besides, the asymmetric growth of  $\text{ReS}_2$ , which leads to its growth into a dendritic morphology, can be suppressed at relatively low temperatures ( $<700$  °C). FETs based on the grown  $\text{ReS}_2$  exhibited superior electrical (mobility of up to  $40 \text{ cm}^2 \text{ V}^{-1} \text{ s}^{-1}$ ) and photoelectrical properties. The high crystal quality and superior anisotropy of  $\text{ReS}_2$ , together with its controllable

growth, endow it with great potential for future applications in high-performance electronic devices.

## 2. Experimental section

### Epitaxial growth and transfer of $\text{ReS}_2$ film

CVD growth was carried out in a single-temperature-zone tubular furnace under atmospheric pressure. Before growth,  $\text{ReO}_3$  powder (purity 99.9%) and sulfur powder (purity 99.5%) were placed at the center and the outside edge ( $\sim 200$  °C) of the hot zone, respectively. Two (or several) pieces of freshly cleaved fluorophlogopite mica substrate (1 cubic centimeter in size) were stacked together to form a microreactor by simply putting one piece onto another piece. The electrostatic force between two mica substrates made them adhere together tightly. Then, they were put onto a ceramic boat containing  $\text{ReO}_3$  powder. Argon was used as a carrier gas with a flow rate of 80 sccm during the whole growth process. The furnace temperature was ramped to the growth temperature (500–800 °C) at  $25 \text{ }^\circ\text{C min}^{-1}$  and then maintained for 3 min for the growth of  $\text{ReS}_2$ . The as-grown  $\text{ReS}_2$  sample was then transferred onto a  $\text{SiO}_2/\text{Si}$  (300 nm) substrate *via* a poly(methyl methacrylate)-mediated transfer process. Hydrofluoric acid (20 wt%) was used as an etchant to delaminate  $\text{ReS}_2$  film from the mica substrate.

### Characterization of grown $\text{ReS}_2$ film

The surface morphologies of  $\text{ReS}_2$  samples were characterized by optical microscopy (Olympus BX51), SEM (Nova NanoSEM 450) and AFM (Bruker Dimension ICON). Raman and fluorescence spectra of different  $\text{ReS}_2$  layers were recorded in a confocal Raman microscopy system (Renishaw). Absorption spectra were recorded using a UV/vis/near infrared spectrometer (Lambda 950). TEM images were obtained with an HRTEM (Tecnai G2 F20; accelerating voltage, 200 kV). The TEM samples were prepared by transferring  $\text{ReS}_2$  film onto lacy carbon film-supported copper grids in a similar method to that described in the last paragraph.

### Device fabrication and electrical measurements

A  $\text{ReS}_2$  sample was transferred onto a  $\text{SiO}_2/\text{Si}$  (300 nm) substrate. Electrical contacts with the  $\text{ReS}_2$  sample were achieved using standard electron beam lithography and thermal evaporation of 5 nm Cr and 50 nm Au. Electrical transport and photoelectric properties were measured in ambient air conditions using an Agilent B2912A source meter unit with a 532 nm laser as a light source. The laser power was adjusted from 430 to  $0.73 \text{ } \mu\text{W mm}^{-2}$  using an optical attenuator (Thorlabs NDC-50C-4M) and was measured using a laser power meter (Thorlabs PM 100D).

## 3. Results and discussion

To synthesize a monolayer  $\text{ReS}_2$  film, a CVD system equipped with a single-zone furnace was employed (Fig. 1a). Rhenium

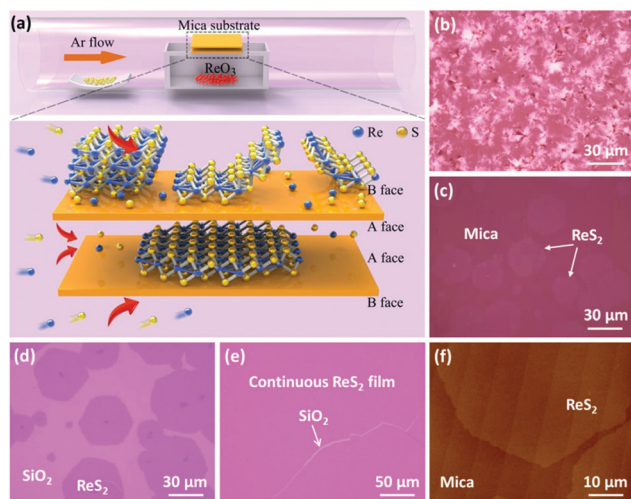


**Fig. 1** (a) Schematic diagram of the space-confined CVD growth of  $\text{ReS}_2$  and the surface reaction during the epitaxial growth process of a  $\text{ReS}_2$  atomic layer on mica. Optical images of  $\text{ReS}_2$  grown on the (b) B face and (c) A face of a mica substrate. (d and e) Optical images of  $\text{ReS}_2$  grown on the A face after being transferred onto a  $\text{SiO}_2/\text{Si}$  (300 nm) substrate. (f) AFM image of as-grown  $\text{ReS}_2$  on a mica substrate.

trioxide ( $\text{ReO}_3$ ) and sulphur (S) were used as the Re and S precursors, respectively, and argon (Ar) was used as a carrier gas during the growth process. The typical growth temperature and growth time were set at 600 °C and 3 min, respectively. As can be imagined,  $\text{ReO}_3$  should be a much better Re precursor for growing  $\text{ReS}_2$  in comparison to Re metal (melting point 3180 °C) and  $\text{NH}_4\text{ReO}_4$  molecules (which bring about low crystal quality), which were used in previous work,<sup>15,16,19</sup> and can ensure high growth efficiency and high crystal quality at low growth temperatures. However, it also faces serious problems: unstable  $\text{ReO}_3$  quickly decomposes into  $\text{Re}_2\text{O}_7$  (which sublimes easily) and  $\text{ReO}_2$  (which is less volatile) *via* a disproportionation reaction (reaction (1)) when the temperature rises to 400 °C (see its thermogravimetric analysis in Fig. S1†).



The very high volatility of  $\text{Re}_2\text{O}_7$  (melting point: 220 °C and boiling point: 360 °C) results in abundant vapor and nucleation sites, which lead to the growth of a large amount of thick 3D flower-like  $\text{ReS}_2$  flakes on the substrate (Fig. 1b). To solve this problem, two pieces of freshly exfoliated mica were stacked together to form an envelope-like structure and placed above the ceramic boat (Fig. 1a). Here, the inner mica surface and the outer mica surface are defined as the A face and B face, respectively. It can be seen that  $\text{ReS}_2$  grown on the B face (Fig. 1b) and A face (Fig. 1c) of each mica substrate exhibits great differences.

As shown in Fig. 1a, when two pieces of the mica substrate were tightly stacked together, the small crevice between them formed a microreactor for the growth of  $\text{ReS}_2$ . The microreactor exerted a space-confining effect in decreasing the concentration of precursors and thus decreased the nucleation density and growth rate of  $\text{ReS}_2$ . As a result, a large-scale  $\text{ReS}_2$  film with hexagonal morphology and a domain size of up to 60  $\mu\text{m}$  could grow on the A faces (Fig. 1c and d), and a continuous uniform  $\text{ReS}_2$  monolayer film could even be obtained (Fig. 1e) when the growth time was prolonged to 8 min. The important role of space confinement in the controlled growth of  $\text{ReS}_2$  was further confirmed by performing *in situ* contrast experiments (Fig. S2†). An AFM image (Fig. 1f) reveals that the grown  $\text{ReS}_2$  has a smooth surface with a thickness of  $\sim 0.73$  nm, which indicates monolayer thickness.<sup>20</sup> Moreover, when several pieces of mica were stacked together to form a multilayer sandwich structure to serve as a growth substrate, a uniform monolayer  $\text{ReS}_2$  film could grow on the A face of each piece of mica, which indicated the high-yield synthesis of  $\text{ReS}_2$  film using this approach. Furthermore, we also synthesized  $\text{ReS}_2$  on a  $\text{SiO}_2$  substrate using a similar growth approach, but only thick flakes and flower-like  $\text{ReS}_2$  were obtained, which were similar to the results obtained in most recent research works.<sup>10,17</sup> The different growth behavior could be understood from an analysis of the surface properties of the growth substrate and the special structure of  $\text{ReS}_2$  itself, as is discussed below.

The Raman spectra of as-grown  $\text{ReS}_2$  films with different thicknesses are shown in Fig. 2a. The primary Raman shifts of the III, IV, V, and VI peaks are located at 152, 161, 212, and 235  $\text{cm}^{-1}$ , respectively, which match well with those of mechanically exfoliated  $\text{ReS}_2$  samples.<sup>21,22</sup> In a similar way to previous findings,<sup>21</sup> only the low Raman shifts of the I and II peaks at 134 and 141  $\text{cm}^{-1}$  display slight sensitivity to the layer number (Fig. S3a†). Photoluminescence (PL) and absorption measurements were performed to determine the band gap of the as-grown  $\text{ReS}_2$  film (Fig. 2b). The energy positions of the PL and absorption peaks match well at about 1.61 eV, which is consistent with the band gap value of monolayer  $\text{ReS}_2$ . In addition, the measured band gap became narrower with an increase in the layer number, ranging from 1.61 eV for a monolayer to 1.48 eV for few layers (Fig. S3b†), which demonstrated the dependence on the layer number of the band gap. All these spectral features of CVD-grown  $\text{ReS}_2$  exhibit a stark contrast to the typical behavior seen in Mo- and W-based TMDs,<sup>23</sup> which is attributed to the interlayer decoupling properties of  $\text{ReS}_2$ .

X-ray photoelectron spectroscopy (XPS) was utilized to confirm the elemental composition and bonding types of the grown  $\text{ReS}_2$  film. Five elements are present in the spectrum that was acquired (Fig. 2c). The signals of Re and S arise from the  $\text{ReS}_2$  sample, those of Si and O originate from the  $\text{SiO}_2$  substrate and that of C arises from residues of PMMA used

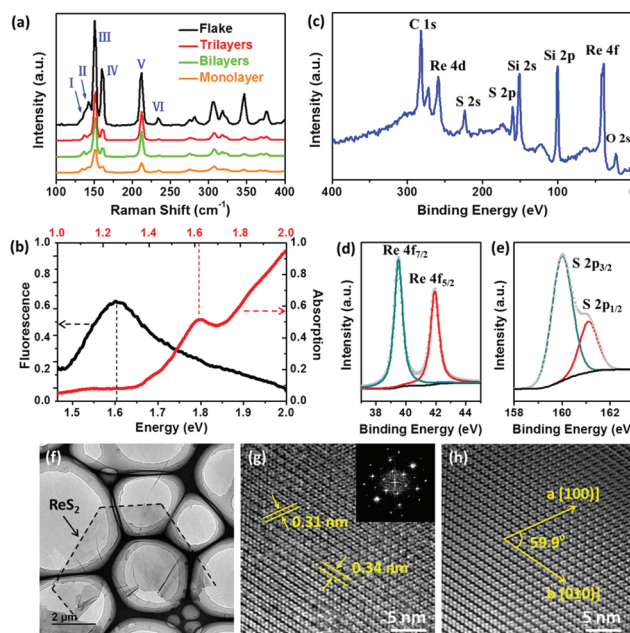


**Fig. 2** Characterization of structure and composition of CVD-grown  $\text{ReS}_2$  film. (a) Raman spectra for thicknesses varying from a monolayer to a thick layer. (b) Fluorescence and absorption spectra of monolayer  $\text{ReS}_2$  film. (c) Full XPS spectrum of  $\text{ReS}_2$  film and detailed signals of the (d) Re 4f and (e) S 2p spectra. (f) Low-resolution TEM image of  $\text{ReS}_2$  supported on a TEM grid. (g) High-resolution TEM image of  $\text{ReS}_2$ ; the inset shows the SAED pattern of  $\text{ReS}_2$ . (h) Fast Fourier transform (FFT) image of (g).

during transfer. The primary peaks at 164.30 and 40.41 eV correspond to S 2p and Re 4f states, respectively. The two characteristic peaks at 38.80 and 41.20 eV are attributed to the Re 4f<sub>7/2</sub> and 4f<sub>5/2</sub> binding energies of Re<sup>4+</sup> (Fig. 2d). The core-level peaks (Fig. 2e) that correspond to the 2p<sub>3/2</sub> and 2p<sub>1/2</sub> binding energies of divalent sulfide ions (S<sup>2-</sup>) are located at 161.20 and 160.00 eV, respectively. In addition, the atomic ratio between Re and S elements is 1 : 1.97, which indicates that the grown ReS<sub>2</sub> is reasonably stoichiometric.

To further analyze the crystallographic structure of the grown ReS<sub>2</sub>, we performed high-resolution transmission electron microscopy (HRTEM) and selected-area electron diffraction (SAED) by transferring ReS<sub>2</sub> onto a TEM grid. Fig. 2f shows a low-magnification TEM image of ReS<sub>2</sub> film, in which a clean uniform membrane can be seen. The distorted 1T structural characteristics of ReS<sub>2</sub> with visible DS-chain lattice fringes of Re are distinctly observed in the HRTEM image (Fig. 2g). The interplanar distances along the *b*-axis and *a*-axis, which correspond to the (010) and (100) lattice planes of ReS<sub>2</sub>, were measured to be 0.34 and 0.31 nm, respectively. The SAED pattern and fast Fourier transform (FFT) image clearly confirm the *a*[100] and *b*[010] orientation of the distorted 1T crystal with an angle of ~59.9° (Fig. 2h), which suggests that our ReS<sub>2</sub> has high crystal quality.

To reveal the unusual growth mechanism of low-lattice-symmetry ReS<sub>2</sub>, we studied its growth behavior on different substrates and at different temperatures. Fig. 3 shows the morphology of ReS<sub>2</sub> obtained on SiO<sub>2</sub> and mica substrates in the same growth conditions and a corresponding schematic diagram of the growth behavior on these two substrates. Obviously, thick flakes and flower-like shapes of ReS<sub>2</sub> tended to grow on the SiO<sub>2</sub> substrate (Fig. 3 and S4†), which occur much more easily in the growth of ReS<sub>2</sub> in comparison to that of traditional TMDs. This unusual growth feature could be understood from the surface properties of the growth substrate and the distorted 1T structure of ReS<sub>2</sub> itself. The rough surface of the SiO<sub>2</sub> substrate with abundant dangling bonds and defects brings about a high energy barrier to the surface migration of adatoms,<sup>24,25</sup> which hinders the free migration of adatoms on the substrate during growth (Fig. 3a). In contrast,

the weak interlayer coupling of ReS<sub>2</sub> allows the free migration of adatoms on its own surface. Thus, thick ReS<sub>2</sub> flakes with small domain sizes are easily grown on a SiO<sub>2</sub> substrate. Besides, flower-like morphology of ReS<sub>2</sub> indicates out-of-plane growth, which is another typical feature of the growth of low-lattice-symmetry 2D materials. As is known, out-of-plane growth occurs occasionally in the growth of traditional TMDs at an extremely high precursor concentration<sup>26,27</sup> but occurs quite easily for ReS<sub>2</sub> even at a low precursor concentration (Fig. 3b and c). We suspect that the anisotropic growth of low-lattice-symmetry ReS<sub>2</sub> induces strain or defects during its initial nucleation period, which makes out-of-plane growth occur much more easily. In addition, the interlayer decoupling of ReS<sub>2</sub> could make the growth of ReS<sub>2</sub> free from the influence of other layers. Thus, the unusual structure and interlayer decoupling of ReS<sub>2</sub> should be the root cause of the out-of-plane growth on the SiO<sub>2</sub> substrate.

In contrast, the flat and inert surface of the mica substrate makes the energy barrier to the surface migration of adatoms on it much lower than that on the SiO<sub>2</sub> substrate.<sup>24</sup> Hence, the atomically flat surface of mica facilitates the migration of adatoms on it during CVD growth (Fig. 3d), in which atoms have a fast diffusion rate and longer diffusion length. This renders the growth of ReS<sub>2</sub> on mica surface-dominated, which is responsible for the nucleation and growth of a ReS<sub>2</sub> film that lies flat on the mica surface. In addition, the weak van der Waals interaction between the surface of mica and adatoms exerts a surface-confining (induction) role during the epitaxial growth process of ReS<sub>2</sub>, which could efficiently suppress out-of-plane growth. As a result, a ReS<sub>2</sub> film with large domains, hexagonal morphology and uniform monolayer thickness could be obtained on the mica substrate (Fig. 3e and f). In this regard, we could control the growth model (in-plane/out-of-plane) to obtain flat 2D ReS<sub>2</sub> films or vertical 3D ReS<sub>2</sub> nanoflowers by choosing appropriate growth substrates. These two types of ReS<sub>2</sub> structure have promising applications in electronic devices and catalysis (and lithium batteries), respectively.<sup>17,28</sup>

Interestingly, the morphology of ReS<sub>2</sub> grown at different temperatures exhibits obvious variations (Fig. 4), changing from regular round and hexagonal shapes to irregular serrated and dendritic shapes with an increase in temperature. Dendritic morphology of ReS<sub>2</sub> indicates an asymmetric growth model, which is a typical growth feature of low-lattice-symmetry 2D materials. This unusual growth model is attributed to the anisotropic interfacial energy induced by the distorted 1T structure.<sup>15</sup> The temperature-modulated evolution of morphology can be understood from the temperature-dependent migration coefficient (*D*) of adatoms on a substrate (see eqn (2)):

$$D \propto e^{-E_m/kT} \quad (2)$$

where *E<sub>m</sub>* is the energy barrier to migration, *k* is Boltzmann's constant and *T* is the substrate temperature.<sup>19,24</sup> At low growth temperatures, atomic diffusion is relatively slow and the attachment and detachment of adatoms at the edges of ReS<sub>2</sub> are limited, which makes epitaxial growth occur in the

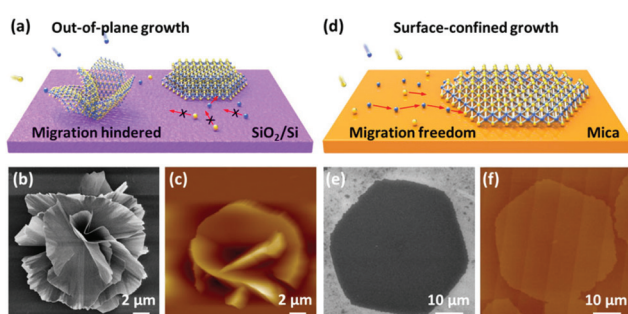


**Fig. 3** Schematic diagrams of the two different growth behaviors of ReS<sub>2</sub> on (a) SiO<sub>2</sub>/Si and (d) mica substrates. (b) SEM and (c) AFM images of ReS<sub>2</sub> film grown on a SiO<sub>2</sub>/Si substrate. (e) SEM and (f) AFM images of a ReS<sub>2</sub> flake grown on a mica substrate.

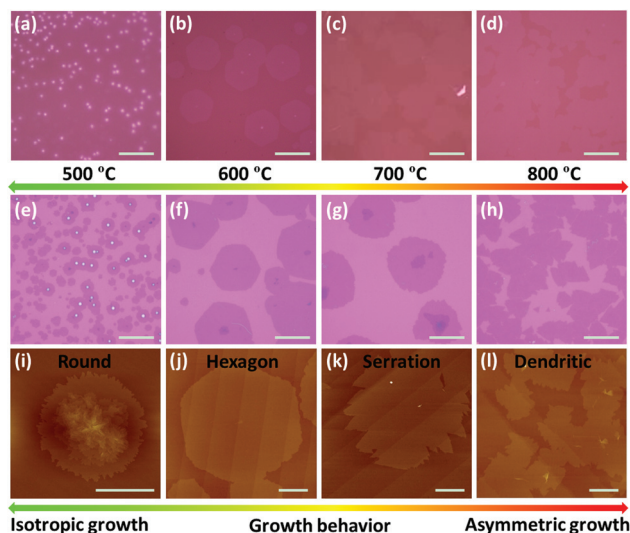


**Fig. 4** Temperature-modulated growth behavior of ReS<sub>2</sub> film. OM images of ReS<sub>2</sub> grown at (a) 500 °C, (b) 600 °C, (c) 700 °C and (d) 800 °C on a mica substrate (the scale bar represents 30 μm). (e–h) Corresponding OM images of ReS<sub>2</sub> film transferred onto a SiO<sub>2</sub>/Si substrate (the scale bar represents 30 μm). (i–l) Corresponding AFM images of as-grown ReS<sub>2</sub> on mica (the scale bar represents 10 μm).

directions of the two crystal axes at nearly the same rate. Thus, symmetric growth is dominant, which allows ReS<sub>2</sub> to grow into regular hexagonal shapes. On the basis of recent studies,<sup>29,30</sup> we know that hexagonal ReS<sub>2</sub> domains should be composed of six subdomains, in which the direction of Re chains changes

by 60° from one subdomain to another. However, at high growth temperatures, atomic diffusion becomes fast and adatoms are enabled to migrate and attach in the highly activated growth direction along the crystal axis where this is energetically favorable. As a consequence, asymmetric growth becomes apparent, which makes ReS<sub>2</sub> grow into an irregular dendritic shape. Our results indicate that the asymmetric growth of this type of material, which brings about irregular morphology of ReS<sub>2</sub>, is reduced markedly when growth occurs at a low temperature (<700 °C), and thus materials with regular morphology can be obtained. Of course, the temperature cannot be excessively low (<500 °C), otherwise amorphous domains would grow on the monolayer surface owing to the reduction in the migration energy of adatoms. Furthermore, the quality of ReS<sub>2</sub> decreases when the growth temperature is below 500 °C (Fig. S5†). Therefore, the morphology and crystal quality of ReS<sub>2</sub> can be effectively controlled by tuning its growth temperature.

Fig. 5a shows a typical structure and OM image of a ReS<sub>2</sub> phototransistor device. The linear source–drain current *versus* voltage ( $I_{\text{ds}}-V_{\text{ds}}$ ) feature suggests ohmic contact between the Cr/Au metal pads and ReS<sub>2</sub> (Fig. 5b). The ReS<sub>2</sub> device exhibits n-type conduction with a current on/off ratio of up to 10<sup>6</sup> and a threshold voltage of –36 V (Fig. 5c). The electron mobility of our ReS<sub>2</sub> device can reach up to 40 cm<sup>2</sup> V<sup>-1</sup> s<sup>-1</sup>, which is calculated from the equation:

$$\mu = \frac{L}{WV_{\text{ds}}C_g} \frac{dI_{\text{ds}}}{dV_{\text{bg}}} \quad (3)$$

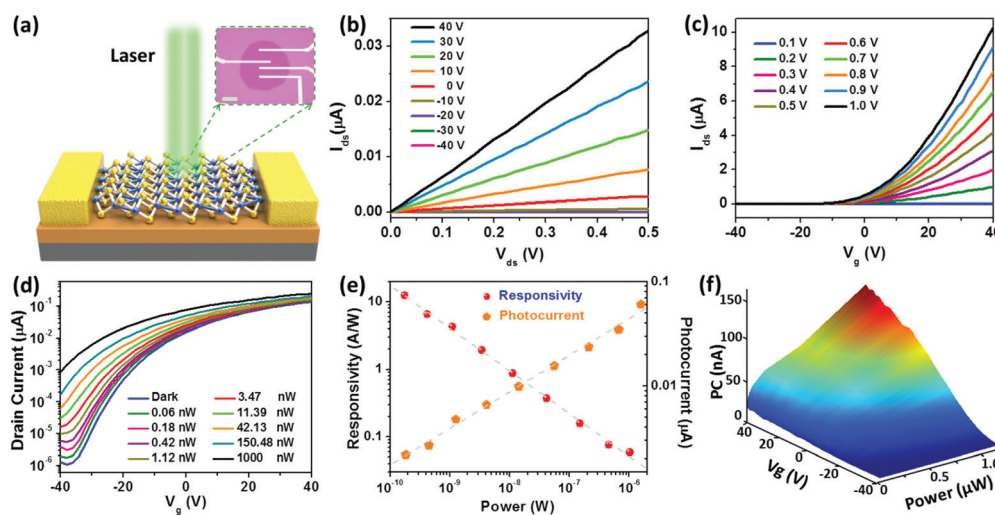


**Fig. 5** Electrical and photoelectrical properties of devices made from CVD-grown monolayer ReS<sub>2</sub> film. (a) Schematic diagram of a back-gated ReS<sub>2</sub> phototransistor. The inset shows an OM image of a typical ReS<sub>2</sub> device on 300 nm SiO<sub>2</sub>/Si (the scale bar represents 10 μm). (b) Source–drain current ( $I_{\text{ds}}$ ) *versus* voltage ( $V_{\text{ds}}$ ) characteristics of the device at various values of the gate voltage ( $V_{\text{g}}$ ). (c) Transfer curve ( $I_{\text{ds}}$  *versus*  $V_{\text{g}}$  curve) for the same device at various values of  $V_{\text{ds}}$ . (d) Transfer curve of a ReS<sub>2</sub> FET (another device) measured under various light irradiation powers at  $V_{\text{ds}} = 0.5$  V. (e) Photocurrent (PC) and responsivity ( $R$ ) as a function of light irradiation power measured at  $V_{\text{ds}} = 0.5$  V and  $V_{\text{g}} = 0$  V. The dotted lines for PC ( $R$ ) are the best fits to the data using the functions  $\text{PC} = P^\beta$  ( $R = P^{\beta-1}$ ), where  $P$  is the effective power of the irradiating light on the device and  $\beta$  is a constant. (f) 3D photocurrent map of the ReS<sub>2</sub> phototransistor with varying values of  $V_{\text{g}}$  and power of light irradiating at  $V_{\text{ds}} = 0.5$  V. The effective power of light is obtained with a device area of 189 μm<sup>2</sup>.

where  $L$ ,  $W$ , and  $C_g$  are the channel length, width, and gate capacitance per unit area, respectively.<sup>31</sup> Notably, this is the highest value of electron mobility recently reported for CVD-grown ReS<sub>2</sub>, and is even comparable with that of mechanically exfoliated ReS<sub>2</sub> flakes (1–50 cm<sup>2</sup> V<sup>-1</sup> s<sup>-1</sup>),<sup>11,12</sup> which highlights the high crystal quality of the grown ReS<sub>2</sub> samples.

As shown in Fig. 5d, the measured values of  $I_{ds}$  as a function of  $V_g$  at various light irradiation powers ( $P$ ) reveal the obvious gate tunability of the photocurrent response of the ReS<sub>2</sub> phototransistor. The photoresponsivity, which is defined as the photocurrent generated per unit power of incident light on the effective area, was estimated to be 12 A W<sup>-1</sup> at an irradiation intensity of 0.05 mW cm<sup>-2</sup> ( $V_{ds} = 0.5$  V and  $V_g = 0$  V). This responsivity is comparable to the results reported for exfoliated thick-layer ReS<sub>2</sub> photodetectors,<sup>10,22,32,33</sup> whereas an even better value would be achieved if the device was tested at large values of  $V_{ds}$  and  $V_g$ , as is discussed below. In addition, the responsivity (photocurrent) is linearly proportional to the power of the incident light,  $R = P^{\beta-1}(I_{ph} = P^{\beta})$  at  $\beta = 0.37$ , as shown in Fig. 5e. This linear relationship indicates that the photocurrent is determined by a photoconductive mechanism. In addition, the photocurrent depends linearly on the value of  $V_{ds}$  and increases gradually with an increase in the power of the incident light (Fig. S6a†). An increase in  $V_{ds}$  reduces the carrier transit time by providing a stronger electric field in the conduction channel, which thus reduces the possibility of carrier recombination. The photoresponse of the ReS<sub>2</sub> device to the switching on and off of light exhibits better temporal resolution (Fig. S6b†). A 3D photocurrent map of the ReS<sub>2</sub> device clearly shows that the photocurrent can be modulated by tuning the value of  $V_g$  (Fig. 5f), where  $V_g$  can modulate the energy barriers between the Fermi level of Au and the conduction band of ReS<sub>2</sub>. Such gate-tunable photoresponse by adjusting the Schottky barriers is important for pixelated imaging applications.

## 4. Conclusions

In summary, we present an approach based on space-confined CVD growth for the controlled synthesis of a large-area highly crystalline uniform monolayer ReS<sub>2</sub> film. The microreaction chamber that was constructed, which exerts a space-confining effect to reduce the nucleation density and growth rate of ReS<sub>2</sub>, is critical for the controlled growth of ReS<sub>2</sub> from a volatile ReO<sub>3</sub> precursor. In addition, the out-of-plane growth and asymmetric growth of low-lattice-symmetry ReS<sub>2</sub> can be suppressed by growing it on a substrate with low surface energy at a relatively low temperature. The high crystal quality, in combination with the superior electrical and photoelectric properties of the CVD-grown ReS<sub>2</sub>, endows it with great potential for use in electronic and optoelectronic devices. Furthermore, our results are beneficial for understanding and controlling the unusual growth behavior of low-lattice-symmetry 2D layered materials.

## Acknowledgements

This work was supported by the National Natural Science Foundation of China (51502167) and the Fundamental Research Funds for the Central Universities (GK201502003).

## Notes and references

- 1 F. N. Xia, H. Wang and Y. C. Jia, *Nat. Commun.*, 2014, **5**, 4458.
- 2 J. X. Wu, N. N. Mao, L. M. Xie, H. Xu and J. Zhang, *Angew. Chem., Int. Ed.*, 2015, **54**, 2366–2369.
- 3 S. Tongay, H. Sahin, C. Ko, A. Luce, W. Fan, K. Liu, J. Zhou, Y. S. Huang, C. H. Ho, J. Y. Yan, D. F. Ogletree, S. Aloni, J. Ji, S. S. Li, J. Li, F. M. Peeters and J. Q. Wu, *Nat. Commun.*, 2014, **5**, 3252.
- 4 S. X. Yang, C. Wang, H. Sahin, H. Chen, Y. Li, S. S. Li, A. Suslu, F. M. Peeters, Q. Liu, J. B. Li and S. Tongay, *Nano Lett.*, 2015, **15**, 1660–1666.
- 5 S. H. Jo, H. Y. Park, D. H. Kang, J. Shim, J. Jeon, S. Choi, M. Kim, Y. Park, J. Lee, Y. J. Song, S. J. Lee and J. H. Park, *Adv. Mater.*, 2016, **28**, 6711–6718.
- 6 L. Hart, S. Dale, S. Hoye, J. L. Webb and D. Wolverson, *Nano Lett.*, 2016, **16**, 1381–1386.
- 7 C. H. Ho, *Opt. Express*, 2005, **13**, 8–19.
- 8 Y. C. Lin, H. P. Komsa, C. H. Yeh, T. Björkman, Z. Y. Liang, C. H. Ho, Y. S. Huang, P. W. Chiu, A. V. Krasheninnikov and K. Suenaga, *ACS Nano*, 2015, **9**, 11249–11257.
- 9 N. R. Pradhan, A. McCreary, D. Rhodes, Z. G. Lu, S. Feng, E. Manousakis, D. Smirnov, R. Namburu, M. Dubey, A. R. Hight Walker, H. Terrones, M. Terrones, V. Dobrosavljevic and L. Balicas, *Nano Lett.*, 2015, **15**, 8377–8384.
- 10 E. Zhang, Y. B. Jin, X. Yuan, W. Y. Wang, C. Zhang, L. Tang, S. S. Liu, P. Zhou, W. D. Hu and F. X. Xiu, *Adv. Funct. Mater.*, 2015, **25**, 4076–4082.
- 11 C. M. Corbet, C. McClellan, A. Rai, S. S. Sonde, E. Tutuc and S. K. Banerjee, *ACS Nano*, 2015, **9**, 363–370.
- 12 E. F. Liu, Y. J. Fu, Y. J. Wang, Y. Q. Feng, H. M. Liu, X. G. Wan, W. Zhou, B. G. Wang, L. B. Shao, C. H. Ho, Y. S. Huang, Z. Y. Cao, L. G. Wang, A. D. Li, J. W. Zeng, F. Q. Song, X. R. Wang, Y. Shi, H. T. Yuan, H. Y. Hwang, Y. Cui, F. Miao and D. Y. Xing, *Nat. Commun.*, 2015, **6**, 6991.
- 13 E. F. Liu, M. S. Long, J. W. Zeng, W. Luo, Y. J. Wang, Y. M. Pan, W. Zhou, B. G. Wang, W. D. Hu, Z. H. Ni, Y. M. You, X. A. Zhang, S. Q. Qin, Y. Shi, K. Watanabe, T. Taniguchi, H. T. Yuan, H. Y. Hwang, Y. Cui, F. Miao and D. Y. Xing, *Adv. Funct. Mater.*, 2016, **26**, 1938–1944.
- 14 F. C. Liu, S. J. Zheng, X. X. He, A. Chaturvedi, J. F. He, W. L. Chow, T. R. Mion, X. L. Wang, J. D. Zhou, Q. D. Fu, H. J. Fan, B. K. Tay, L. Song, R. H. He, C. Kloc, P. M. Ajayan and Z. Liu, *Adv. Funct. Mater.*, 2015, **26**, 1169–1177.
- 15 K. Keyshar, Y. J. Gong, G. Ye, G. Brunetto, W. Zhou, D. P. Cole, K. Hackenberg, Y. He, L. Machado, M. Kabbani,

- A. H. C. Hart, B. Li, D. S. Galvao, A. George, R. Vajtai, C. S. Tiwary and P. M. Ajayan, *Adv. Mater.*, 2015, **27**, 4640–4648.
- 16 X. X. He, F. C. Liu, P. Hu, W. Fu, X. L. Wang, Q. S. Zeng, W. Zhao and Z. Liu, *Small*, 2015, **11**, 5423–5429.
- 17 J. Gao, L. Li, J. W. Tan, H. Sun, B. C. Li, J. C. Idrobo, C. V. Singh, T. M. Lu and N. Koratkar, *Nano Lett.*, 2016, **16**, 3780–3787.
- 18 N. Al-Dulaimi, E. A. Lewis, D. J. Lewis, S. K. Howell, S. J. Haigh and P. O'Brien, *Chem. Commun.*, 2016, **52**, 7878–7881.
- 19 F. F. Cui, C. Wang, X. B. Li, G. Wang, K. Q. Liu, Z. Yang, Q. L. Feng, X. Liang, Z. Y. Zhang, S. Z. Liu, Z. Lei, Z. H. Liu, H. Xu and J. Zhang, *Adv. Mater.*, 2016, **28**, 5019–5024.
- 20 D. Wolverson, S. Crampin, A. S. Kazemi, A. Ilie and S. J. Bending, *ACS Nano*, 2014, **8**, 11154–11164.
- 21 D. A. Chenet, O. B. Aslan, P. Y. Huang, C. Fan, A. M. van der Zande, T. F. Heinz and J. C. Hone, *Nano Lett.*, 2015, **15**, 5667–5672.
- 22 R. He, J. A. Yan, Z. Y. Yin, Z. P. Ye, G. H. Ye, J. Cheng, J. Li and C. H. Lui, *Nano Lett.*, 2016, **16**, 1404–1409.
- 23 A. Splendiani, L. Sun, Y. Zhang, T. Li, J. Kim, C. Y. Chim, G. Galli and F. Wang, *Nano Lett.*, 2010, **10**, 1271–1275.
- 24 Q. S. Wang, K. Xu, Z. X. Wang, F. Wang, Y. Huang, M. Safdar, X. Y. Zhan, F. M. Wang, Z. Z. Cheng and J. He, *Nano Lett.*, 2015, **15**, 1183–1189.
- 25 H. Li, J. Cao, W. S. Zheng, Y. L. Chen, D. Wu, W. H. Dang, K. Wang, H. L. Peng and Z. F. Liu, *J. Am. Chem. Soc.*, 2012, **134**, 6132–6135.
- 26 L. M. Zhang, K. Liu, A. B. Wong, J. Kim, X. P. Hong, C. Liu, T. Cao, S. G. Louie, F. Wang and P. D. Yang, *Nano Lett.*, 2014, **14**, 6418–6423.
- 27 L. Chen, B. Liu, A. N. Abbas, Y. Q. Ma, X. Fang, Y. H. Liu and C. W. Zhou, *ACS Nano*, 2014, **8**, 11543–11551.
- 28 Q. Zhang, S. J. Tan, R. G. Mendes, Z. T. Sun, Y. T. Chen, X. Kong, Y. H. Xue, M. H. Rummeli, X. J. Wu, S. L. Chen and L. Fu, *Adv. Mater.*, 2016, **28**, 2616–2623.
- 29 M. Hafeez, L. Gan, H. Q. Li, Y. Ma and T. Y. Zhai, *Adv. Mater.*, 2016, **28**, 8296–8301.
- 30 K. Wu, B. Chen, S. Yang, G. Wang, W. Kong, H. Cai, T. Aoki, E. Soignard, X. Marie, A. Yano, A. Suslu, B. Urbaszek and S. Tongay, *Nano Lett.*, 2016, **16**, 5888–5894.
- 31 H. Xu, J. X. Wu, Q. L. Feng, N. N. Mao, C. M. Wang and J. Zhang, *Small*, 2014, **10**, 2300–2306.
- 32 S. X. Yang, S. Tongay, Q. Yue, Y. T. Li, B. Li and F. Y. Lu, *Sci. Rep.*, 2014, **4**, 5442.
- 33 F. C. Liu, S. J. Zheng, A. Chaturvedi, V. Zolyomi, J. D. Zhou, Q. D. Fu, C. Zhu, P. Yu, Q. S. Zeng, N. D. Drummond, H. J. Fan, C. Kloc, V. I. Fal'ko, X. X. He and Z. Liu, *Nanoscale*, 2016, **8**, 5826–5834.